

## Simulation of a Crack Detection Method for Concrete Structures using SH Waves

L. Godinho<sup>1,4</sup>, D. Dias-da-Costa<sup>2,4</sup>, E. Júlio<sup>3,5</sup> and P. Areias<sup>3,6</sup>

<sup>1</sup>CICC, Coimbra, Portugal, <sup>2</sup>INESC Coimbra, Portugal, <sup>3</sup>ICIST, Lisboa, Portugal

<sup>4</sup>Department of Civil Engineering, University of Coimbra, Portugal

<sup>5</sup>Department of Civil Engineering, Instituto Superior Técnico  
Technical University of Lisbon, Portugal

<sup>6</sup>Physics Department, University of Évora, Portugal

### Abstract

The cost of rehabilitation works increases exponentially with time. Therefore, the development of on-site non-destructive tests for early detection of damage in concrete structures is an extremely important goal. However, in spite of the recent new technological developments, current assessment techniques are still based on visual inspections and are therefore only suitable for mapping major damages.

An innovative procedure aiming to detect cracking at an early stage using propagation of ultrasonic waves is herein numerically analysed. Two advanced models were applied to simulate, first, the process of crack propagation and, next, the propagation of ultrasonic waves in a progressively damaged structure. Results are promising and enforce the feasibility of developing ultrasonic equipment for on-site application and, thus, of carrying on with an experimental validation of the present study.

**Keywords:** wave propagation; non-destructive testing; embedded elements; strong discontinuities; frequency domain; boundary elements.

## 1 Introduction

The possibility of detecting damage in concrete structures early is extremely important, since the cost of rehabilitation works increases exponentially with time. This is not only true for noteworthy structures, such as bridges or dams, but also for regular buildings. However, in spite of the technological developments, structural health assessment is currently mostly based in visual inspections and non-destructive testing which are unable to identify internal damages. More recently, new technologies became available for damage assessment, which are based on the ambient vibration of the structure and correlating the dynamic properties with important damages. Nevertheless, these procedures are only suitable for major damages and not for early assessment [1].

This paper addresses the development of a new approach based on the propagation of ultrasonic waves in a structure for early damage detection. For that purpose a numerical approach has been selected which combines two innovative algorithms to perform a close to reality simulation of the: i) process of crack propagation; and ii) propagation of ultrasonic waves in the progressively damaged structure.

To illustrate the results computed by the described methodology, a representative numerical simulation has been selected, corresponding to a three-point bending beam, for which experimental tests up to failure allowed validating the numerical model concerning crack propagation. These results are then used to simulate the wave propagation and to conclude on the feasibility of the proposed method, in which case a prototype of the ultrasonic equipment will be developed for experimental validation.

## 2 Numerical models

The process of crack formation is modelled with a strong embedded discrete crack approach using enriched finite elements [2-4]. This variationally consistent formulation has been selected due to: i) the possibility of introducing a discontinuity into the finite element mesh irrespective to the boundaries of the enriched finite element; ii) having the additional degrees of freedom placed at the discontinuity and therefore strictly related to the damage of the structure; iii) the possibility of adequately simulating the kinematics of the crack, including both rigid body motion and stretching opening modes; and, more importantly, iv) being a conforming finite element approach which allows maintaining the discontinuity edges fully compatible with the remaining finite element mesh.

Regarding the ultrasonic wave propagation, most existing works deal with full elastic wave propagation (see, e.g. [5] or [6]), and SH waves have not been widely used in ultrasonic applications. This fact is related with technical limitations imposed by the coupling between the probe and the structure. However, when it is possible to correctly ensure this coupling, the use of SH waves has important practical advantages since these waves: i) do not mode convert at oblique incidence on free surfaces; and ii) exhibit slower propagation velocities when compared to P waves, allowing lower frequencies to be adopted for the same resolution. Works by Grahn [7] or by Cegla [8] address this subject, investigating the case of anisotropic plates and of structures exhibiting cracks in inaccessible regions.

To analyse the propagation of SH waves, a boundary element (BEM) model with domain decomposition is used, following the formulation proposed, for example, in [9]. In this model, the boundaries of the propagation domain are discretised and the medium is separated in two subregions, in order to avoid numerical problems along the cracked interface. Computational efficiency is achieved by using an iterative strategy for performing the coupling of subdomains (based on the works of Soares et al. [10]) which leads to smaller matrices describing the behaviour of each subregion.

## 2.1 Crack propagation

This section briefly presents the formulation adopted for the simulation of crack propagation (more details are provided in [11] and [2-4]): the kinematics of the strong discontinuity and the corresponding variational formulation are presented in Section 2.1.1; the discretised equations are derived in Section 2.1.2; and, finally, crack propagation issues are discussed in 2.1.3.

### 2.1.1 Kinematics and variational formulation of a strong discontinuity

Consider an elastic domain  $\Omega$  with an external boundary  $\Gamma$  and an internal boundary, which is the discontinuity  $\Gamma_d$ , dividing the domain in two subregions:  $\Omega^+$  and  $\Omega^-$  (see Figure 1).

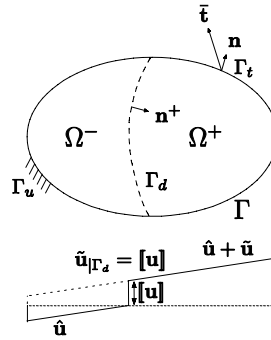


Figure 1: Domain  $\Omega$  crossed by a strong discontinuity  $\Gamma_d$  and 1-D representation of displacement.

A quasi-static loading of body forces  $\bar{\mathbf{b}}$ , natural boundary conditions  $\bar{\mathbf{t}}$  distributed on the external boundary  $\Gamma_t$  and the essential boundary conditions  $\bar{\mathbf{u}}$  prescribed at the boundary  $\Gamma_u$ , are applied to the body. The vector  $\mathbf{n}$  is orthogonal to the boundary surface, pointing outwards, whilst  $\mathbf{n}^+$  is orthogonal to the discontinuity and pointing inwards  $\Omega^+$ .

The total displacement  $\mathbf{u}$  is composed by the sum of two parts: i) the regular displacement field  $\hat{\mathbf{u}}$ ; and ii) the enhanced displacement field  $\tilde{\mathbf{u}}$ , induced by the jumps at the discontinuity:

$$\mathbf{u}(\mathbf{x}) = \hat{\mathbf{u}}(\mathbf{x}) + \mathcal{H}_{\Gamma_d} \tilde{\mathbf{u}}(\mathbf{x}), \quad (1)$$

where  $\mathcal{H}_{\Gamma_d}$  is the standard Heaviside function.

The jump at the discontinuity is obtained by evaluating the enhanced displacement field along the discontinuity:

$$[[\mathbf{u}]] = \left( \mathbf{u}^+ - \mathbf{u}^- \right)_{|\Gamma_d} = \tilde{\mathbf{u}}_{|\Gamma_d}. \quad (2)$$

For small displacements, the strain field is:

$$\boldsymbol{\varepsilon} = \nabla^s \mathbf{u} = \nabla^s \hat{\mathbf{u}} + \mathcal{H}_{\Gamma_d} \nabla^s \tilde{\mathbf{u}} + \delta_{\Gamma_d} \left( [[\mathbf{u}]] \otimes \mathbf{n}^+ \right)^s \quad \text{in } \Omega, \quad (3)$$

where  $(\cdot)^s$  is the symmetric part of  $(\cdot)$  and  $\otimes$  is the dyadic product.

For the problem under consideration, the principle of virtual work can be written as [3]:

$$-\int_{\Omega \setminus \Gamma_d} (\nabla^s \delta \mathbf{u}) : \boldsymbol{\sigma}(\boldsymbol{\varepsilon}) d\Omega - \int_{\Gamma_d} \delta [[\mathbf{u}]] \cdot \mathbf{t}^+ d\Gamma + \int_{\Omega \setminus \Gamma_d} \delta \mathbf{u} \cdot \bar{\mathbf{b}} d\Omega + \int_{\Gamma_t} \delta \mathbf{u} \cdot \bar{\mathbf{t}} d\Gamma = 0. \quad (4)$$

### 2.1.2 Discretised equations

Consider a finite element partition of the 2D domain  $\Omega$ . Each enriched finite element  $\Omega^e$ , with  $n$  nodes, is crossed by a straight discontinuity  $\Gamma_d^e$  dividing it in two subdomains. The adopted conventions are represented in Figure 2.

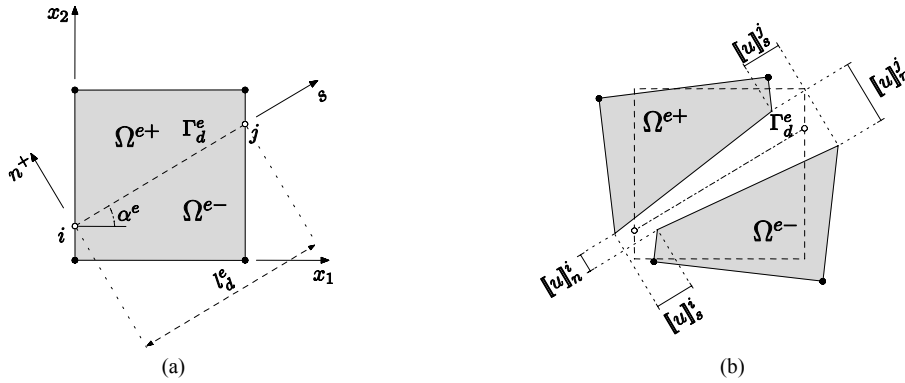


Figure 2: Domain  $\Omega^e$  crossed by a strong discontinuity  $\Gamma_d^e$ : (a) definitions; and (b) general opening.

The following equation provides the approximation of the displacement field for each enriched finite element:

$$\mathbf{u}^e = \mathbf{N}^e(\mathbf{x}) \left[ \mathbf{a}^e + \left( \mathcal{H}_{\Gamma_d} \mathbf{I} - \mathbf{H}_{\Gamma_d}^e \right) \tilde{\mathbf{a}}^e \right] \quad \text{if } \mathbf{x} \in \Omega^e \setminus \Gamma_d^e, \quad (5)$$

$$[[\mathbf{u}]]^e = \mathbf{u}^{e+} - \mathbf{u}^{e-} = \mathbf{N}^e(\mathbf{x}) \tilde{\mathbf{a}}^e \quad \text{at } \Gamma_d^e, \quad (6)$$

where  $\mathbf{N}^e$  contains the element shape functions,  $\mathbf{a}^e$  are the total nodal degrees of freedom related to  $\mathbf{u}^e$ ,  $\tilde{\mathbf{a}}^e$  are the enhanced nodal degrees of freedom related to  $\tilde{\mathbf{u}}^e$ ,  $\mathbf{H}_{\Gamma_d}^e$  is a  $(2n \times 2n)$  diagonal matrix with components equal to '1' for nodal degrees of freedom in  $\Omega^{e+}$  and '0' otherwise.

In order to capture the kinematics of the discontinuity regarding both rigid body motion and stretching of  $\Omega^+$  over  $\Omega^-$ , two additional nodes are placed at the edges of each enriched element (see Figure 2). Therefore, the enhanced nodal degrees of freedom become:

$$\tilde{\mathbf{a}}^e = \mathbf{M}_w^{ek*} \mathbf{w}^{e*}, \quad (7)$$

where  $\mathbf{w}^{e*}$  is a vector formed by juxtaposing by rows the additional degrees of freedom resulting from the contribution of the following  $n_{el}$  enriched elements: i) element ‘ $e$ ’; and ii) all remaining enriched elements sharing at least one node with element ‘ $e$ ’. Matrix  $\mathbf{M}_w^{ek*}$  has also the contribution of all these enriched elements, such that each row,  $\mathbf{M}_w^{ei*}$  is in direct correspondence to the  $i$ -node of the element ‘ $e$ ’ and can be computed by:

$$\mathbf{M}_w^{ei*} = \mathbf{M}_w^e + \sum_{j=1, j \neq e}^{n_{el}} \{ \mathbf{M}_w^j - \mathbf{M}_w^e \} \boldsymbol{\beta}^j, \quad (8)$$

where  $\mathbf{M}_w^e$  is:

$$\mathbf{M}_w^e = \mathbf{M}_{R_w}^e + \mathbf{M}_{nR_w}^e, \quad (9)$$

with

$$\mathbf{M}_{R_w}^e = \begin{bmatrix} 1 - \frac{(x_2 - x_2^i) \sin \alpha^e}{l_d^e} & \frac{(x_2 - x_2^i) \cos \alpha^e}{l_d^e} & \frac{(x_2 - x_2^i) \sin \alpha^e}{l_d^e} & -\frac{(x_2 - x_2^i) \cos \alpha^e}{l_d^e} \\ \frac{(x_1 - x_1^i) \sin \alpha^e}{l_d^e} & 1 - \frac{(x_1 - x_1^i) \cos \alpha^e}{l_d^e} & -\frac{(x_1 - x_1^i) \sin \alpha^e}{l_d^e} & \frac{(x_1 - x_1^i) \cos \alpha^e}{l_d^e} \end{bmatrix}, \quad (10)$$

$$\mathbf{M}_{nR_w}^e = \begin{bmatrix} \frac{s_n^e [1 + \cos(2\alpha^e)]}{2} & \frac{s_n^e [\sin(2\alpha^e)]}{2} & \frac{s_n^e [1 + \cos(2\alpha^e)]}{2} & \frac{s_n^e [\sin(2\alpha^e)]}{2} \\ \frac{s_n^e [\sin(2\alpha^e)]}{2} & \frac{s_n^e [1 - \cos(2\alpha^e)]}{2} & \frac{s_n^e [\sin(2\alpha^e)]}{2} & \frac{s_n^e [1 - \cos(2\alpha^e)]}{2} \end{bmatrix} \quad (11)$$

and

$$s_n^e = \frac{s(\mathbf{x}_i)}{l_d^e} = (x_1 - x_1^i) \frac{\cos(\alpha^e)}{l_d^e} + (x_2 - x_2^i) \frac{\sin(\alpha^e)}{l_d^e}, \quad (12)$$

where  $\mathbf{x} = (x_1, x_2)$  is the global position of any material point inside the finite element,  $\mathbf{x}^i = (x_1^i, x_2^i)$  is the global position of the tip ‘ $i$ ’ (Figure 2),  $l_d^e$  is the length

of the discontinuity  $\Gamma_d^e$  measured along the local frame  $\bar{s}$  and ‘ $\alpha^e$ ’ is the discontinuity angle defined in Figure 2.

It is stressed that  $\mathbf{M}_{R_w}^e$  is the rigid-body part, which includes both normal and constant shear jump components, and  $\mathbf{M}_{nR_w}^e$  is the non-rigid stretching part along the discontinuity  $\Gamma_d^e$  (see [3] for more details).

$\boldsymbol{\beta}^j$  is a diagonal matrix computed at each node ‘ $j$ ’, containing  $\beta_{x_i}^j$  terms for both directions  $(x_1, x_2)$ , representing a measure of the relative stiffness contribution of each enriched element for the enhanced displacement field:

$$\beta_{x_i}^j = \frac{K_{i,x_i}^j}{\sum_{k=1}^{n_{el}} K_{i,x_i}^k},$$

where  $K_{i,x_i}^j$  is the stiffness matrix component of the bulk for element ‘ $j$ ’ for direction  $x_i$  (see Figure 2). Therefore, a mutual dependence between jumps and bulk deformation is built, leading to a fully compatible formulation.

The strain field is approximated using the standard strain-displacement matrix,  $\mathbf{B}^e$ :

$$\boldsymbol{\varepsilon}^e = \mathbf{B}^e(\mathbf{x}) \left[ \mathbf{a}^e + \left( \mathcal{H}_{\Gamma_d} \mathbf{I} - \mathbf{H}_{\Gamma_d}^e \right) \mathbf{M}_w^{ek*} \mathbf{w}^{e*} \right] \quad \text{in } \Omega^e \setminus \Gamma_d^e. \quad (13)$$

The incremental stress field and incremental traction at the discontinuity are given by:

$$d\boldsymbol{\sigma}^e = \mathbf{D}^e \mathbf{B}^e(\mathbf{x}) \left[ d\mathbf{a}^e + \left( \mathcal{H}_{\Gamma_d} \mathbf{I} - \mathbf{H}_{\Gamma_d}^e \right) \mathbf{M}_w^{ek*} d\mathbf{w}^{e*} \right] \quad \text{in } \Omega^e \setminus \Gamma_d^e, \quad (14)$$

and

$$d\mathbf{t}^e = \mathbf{T}^e d[[\mathbf{u}]]^e = \mathbf{T}^e \mathbf{N}^e(\mathbf{x}) \mathbf{M}_w^{ek*} \mathbf{w}^{e*} \quad \text{at } \Gamma_d^e, \quad (15)$$

where  $\mathbf{D}^e$  and  $\mathbf{T}^e$  are, respectively, the bulk and the discontinuity constitutive matrices.

Finally, by using the previous equations in equation (4) and by progressively taking: i)  $\delta d\mathbf{w}^{e*} = \mathbf{0}$ ; and ii)  $\delta d\mathbf{a}^e = \mathbf{0}$ , the following system of equations is obtained:

$$\mathbf{K}_{aa}^e d\mathbf{a}^e + \mathbf{K}_{aw}^e d\mathbf{w}^{e*} = d\hat{\mathbf{f}}^e, \quad (16)$$

$$\mathbf{K}_{wa}^e d\mathbf{a}^e + \left( \mathbf{K}_{ww}^e + \mathbf{K}_d^e \right) d\mathbf{w}^{e*} = d\mathbf{f}_w^e \quad (17)$$

where:

$$\mathbf{K}_{aa}^e = \int_{\Omega^e \setminus \Gamma_d^e} \mathbf{B}^{eT} \mathbf{D}^e \mathbf{B}^e d\Omega^e, \quad \mathbf{K}_{aw}^e = \int_{\Omega^e \setminus \Gamma_d^e} \mathbf{B}^{eT} \mathbf{D}^e \mathbf{B}_w^e d\Omega^e,$$

$$\mathbf{K}_{wa}^e = \int_{\Omega^e \setminus \Gamma_d^e} \mathbf{B}_w^{eT} \mathbf{D}^e \mathbf{B}^e d\Omega^e, \quad \mathbf{K}_{ww}^e = \int_{\Omega^e \setminus \Gamma_d^e} \mathbf{B}_w^{eT} \mathbf{D}^e \mathbf{B}_w^e d\Omega^e, \quad \mathbf{K}_d^e = \int_{\Gamma_d^e} \mathbf{N}_w^{eT} \mathbf{T}^e \mathbf{N}_w^e d\Gamma^e,$$

$$\mathbf{B}_w^e = \mathbf{B}^e \left( \mathcal{H}_{\Gamma_d} \mathbf{I} - \mathbf{H}_{\Gamma_d}^e \right) \mathbf{M}_w^{ek*}, \quad \mathbf{N}_w^e = \mathbf{N}^e \left( \mathcal{H}_{\Gamma_d} \mathbf{I} - \mathbf{H}_{\Gamma_d}^e \right) \mathbf{M}_w^{ek*},$$

$$d\hat{\mathbf{f}}^e = \int_{\Omega^e \setminus \Gamma_d^e} \mathbf{N}^{eT} \bar{\mathbf{b}}^e d\Omega^e + \int_{\Gamma_t^e} \mathbf{N}^{eT} \bar{\mathbf{t}}^e d\Gamma \quad \text{and} \quad d\mathbf{f}_w^e = \int_{\Omega^e \setminus \Gamma_d^e} \mathbf{N}_w^{eT} \bar{\mathbf{b}}^e d\Omega^e + \int_{\Gamma_t^e} \mathbf{N}_w^{eT} \bar{\mathbf{t}}^e d\Gamma.$$

### 2.1.3 Crack propagation

It is assumed that the discontinuity is straight and crosses an entire parent element and, therefore, the crack tip is always located at the element edge. Only one crack is allowed to exist inside each enriched element. Furthermore, each new embedded discontinuity can only be inserted: i) at the crack tip; or ii) at new element if outside the neighbourhood of existing crack tips (provided by a radius of influence centred at each crack tip with a value of three to five times the maximum aggregate size). Crack path continuity is enforced using the algorithm presented in [11], whereas the direction of propagation is provided using a Rankine criterion, according to which cracking occurs perpendicularly to the direction of maximum tensile stress [2].

## 2.2 SH wave propagation

In the frequency domain, the SH wave field ( $u(\mathbf{x})$ , with  $\mathbf{x}$  being a domain point with coordinates  $(x_1, x_2)$ ) within a generic homogeneous medium of density ' $\rho$ ' and propagation velocity ' $c_s$ ', and assuming null initial conditions, can be described by the governing partial differential equation

$$\nabla^2 u(\mathbf{x}) + \rho \omega^2 u(\mathbf{x}) = 0, \quad (18)$$

' $\omega$ ' being the frequency, in rad/s.

The analytical solution of this equation can be written in an explicit form only in a limited number of situations, mainly where the geometry is simple. However, complex domains with internal boundaries and varying properties can be analysed using different numerical methods. The BEM is herein adopted with this aim.

### 2.2.1 Boundary Element Model

Consider a finite homogeneous domain of density, with the properties ' $\rho$ ' and ' $c_s$ ' indicated in the previous section, limited by an external boundary  $\Gamma$ . In the absence of any distributed domain load and considering a virtual unit point pressure load oscillating at an angular frequency ' $\omega$ ' acting at point  $\mathbf{x}_0$ , the following boundary integral equation may be written:

$$c_p u(\mathbf{x}_0) = \int_{\Gamma} G(\mathbf{x}, \mathbf{x}_0) v(\mathbf{x}, \vec{n}) d\Gamma - \int_{\Gamma} H(\mathbf{x}, \mathbf{x}_0, \vec{n}) u(\mathbf{x}) d\Gamma + u_{inc}(\mathbf{x}_0, \mathbf{x}_f), \quad (19)$$

where ‘ $u$ ’ and ‘ $v$ ’ represent the displacement and its first derivative along direction  $\vec{n}$ ,  $G(\mathbf{x}, \mathbf{x}_0)$ ,  $H(\mathbf{x}, \mathbf{x}_0, \vec{n})$  are, respectively, the Green’s functions for anti-plane displacement and its first spatial derivative along the same direction  $\vec{n}$ ;  $u_{inc}(\mathbf{x}_f, \mathbf{x}_0)$  represents the incident displacement field generated by a possible point load located within the domain at  $\mathbf{x}_f$ ;  $c_p$  is a constant which takes the value 0.5 for a point over a smooth boundary, and the value 1 for a point within the domain.

Considering an infinite medium, the relevant Green’s function can be defined by:

$$G(\mathbf{x}, \mathbf{x}_0) = -\frac{i}{4} H_0^{(2)} \left( \frac{\omega}{\alpha_2} \sqrt{(x-x_0)^2 + (y-y_0)^2} \right), \quad (20)$$

where  $H_0^{(2)}(\dots)$  is the Hankel function of the second type and order 0.

After discretising the boundary  $\Gamma$  into  $N_{be}$  segments (elements), equation (2) may be written as

$$c_p u(\mathbf{x}_0) = \sum_{j=1}^{N_{be}} \int_{\Gamma_j} G(\mathbf{x}, \mathbf{x}_0) v(\mathbf{x}, \vec{n}) d\Gamma_j - \sum_{j=1}^{N_{be}} \int_{\Gamma_j} H(\mathbf{x}, \mathbf{x}_0, \vec{n}) u(\mathbf{x}) d\Gamma_j + u_{inc}(\mathbf{x}_0, \mathbf{x}_f). \quad (21)$$

The load is applied sequentially at all nodal points to establish  $N_{be}$  equations. The necessary integrations along the boundary can generally be performed by means of Gaussian quadrature. To ensure that the method is accurate, when the loaded element coincides with the integrated element the resulting singular integration should be performed analytically.

### 2.2.2 Iterative coupling between subdomains

The above defined numerical BEM model can be used directly to model a single closed domain, or it can be applied separately to various subdomains, and then imposing the relevant boundary conditions. For the latter case, illustrated in Figure 3, the boundary conditions along the interface between the two subdomains correspond to continuity of the displacement and of its first derivative along the normal direction to the common boundary between domains.

The strategy of domain decomposition in the BEM is not new, and is typically used whenever material discontinuities occur. However, it is also useful when a crack or a thin structure exists, for which the direct application of the BEM originates degenerate equation systems. Indeed, for those cases, either a special formulation of the method (usually referred as BEM-TBEM), or a domain decomposition, separating the model in two independent regions, must be used.

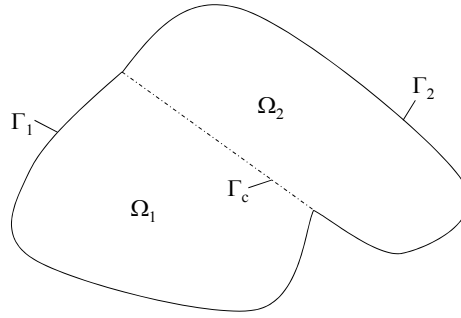


Figure 3: System with two subdomains connected by boundary  $\Gamma_c$ .

For the case of domain decomposition, the problem is usually tackled making use of a single system of equations, coupling the two subdomains. Here, the problem is addressed using a different strategy, making use of iterative coupling between two separate problems to achieve the solution. For that purpose, the strategy of a Neumann-to-Dirichlet iterative process is followed, with the following sequence:

- 1) the response is first computed for domain  $\Omega_1$  imposing null values for  $v(\mathbf{x}, \bar{n})$  along  $\Gamma_c$ ;
- 2) the values of  $u(\mathbf{x})$  along  $\Gamma_c$  are then calculated and imposed as boundary conditions for the problem in  $\Omega_2$ ;
- 3) the response in  $\Omega_2$  is then calculated, and new values of  $v(\mathbf{x}, \bar{n})$  along  $\Gamma_c$  is computed;
- 4) these values of  $v(\mathbf{x}, \bar{n})$  along  $\Gamma_c$  are, once again, imposed as boundary conditions to the problem in  $\Omega_1$ ;
- 5) the process goes back to point 2), until convergence is attained.

The criteria used here for convergence is related to the maximum relative discrepancy between the values of  $u(\mathbf{x})$  along  $\Gamma_c$  calculated for the two subdomains, considering that convergence is attained when this value reaches  $10^{-5}$ . Details on the iterative process can be found in Soares et al. [10].

### 2.2.3 Verification of the model

To verify the BEM with the iteratively coupled subdomains we consider the case of a rectangular structure, with dimensions of 400 mm by 100 mm, incorporating a discontinuity, as represented in Figure 4a. The propagation velocity within the solid medium is 2489.6 m/s, and its density is 2500 kg/m<sup>3</sup>. The system is illuminated by a source located at (50mm; 50mm), and the response is calculated for a frequency of 50 kHz; the model is discretised using 8 boundary elements per wavelength. Figure 4b-c illustrates the displacements (both real and imaginary parts) calculated at lines of receivers located 25 mm and 75 mm above the bottom of the model, using both the iterative model and the standard BEM model. As can be seen, the two results match very well, and indicate a good behaviour of the iterative process, with a strong jump of

displacements being registered when the receiver's line crosses the material discontinuity.

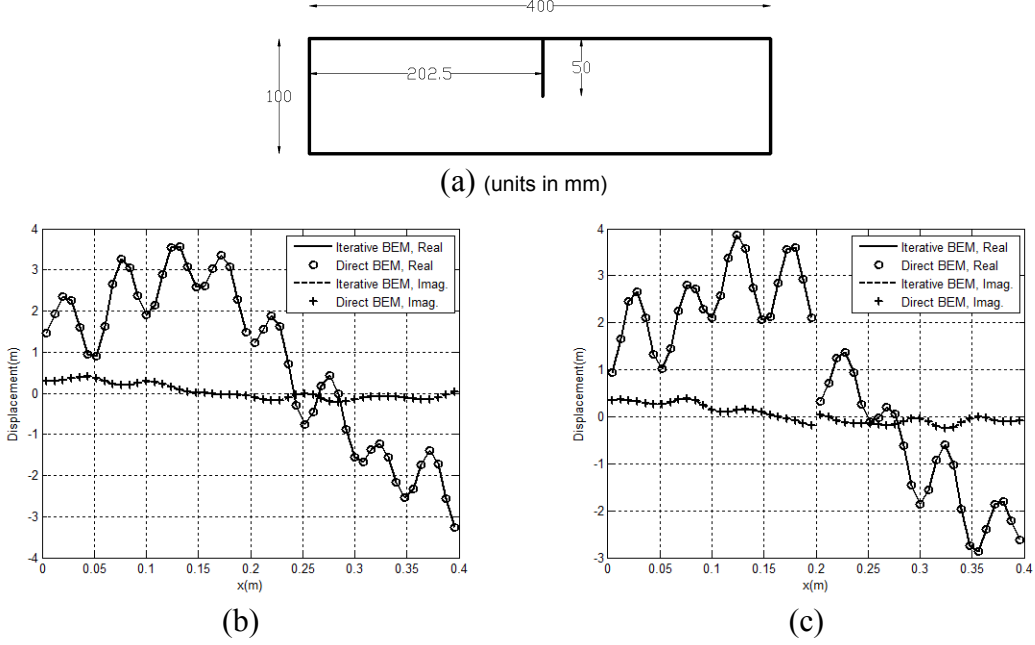


Figure 4: Results for the verification model (a), for 50 kHz, considering lines of receivers placed 25mm (b) and 75mm (c) above the bottom of the model.

## 2.2.4 Calculation of time signals

The above described formulation allows obtaining the pressure response in the frequency domain. Responses in the time domain are obtained using a fast inverse Fourier transform in the frequency domain, considering that the source emits a Ricker wavelet, defined as

$$u(\tau) = A(l - 2\tau^2)e^{-\tau^2}, \quad (22)$$

where  $A$  is the amplitude,  $\tau = (t - t_s)/t_o$  and  $t$  denotes time;  $t_s$  is the time when the maximum occurs, while  $\pi t_o$  is the characteristic (dominant) period of the wavelet. The corresponding Fourier transform is

$$U(\omega) = A \left[ 2\sqrt{\pi} t_o e^{-i\omega t_s} \right] \Lambda^2 e^{-\Lambda^2}, \quad (23)$$

in which  $\Lambda = \omega t_o / 2$ . This wavelet is widely used in different types of analysis, since it decays rapidly, both in the time and in the frequency domains, reducing the computational effort and allowing easier interpretation of the computed time series and synthetic waveforms.

As stated before, the Fourier transformations are obtained by discrete summations over frequencies. Mathematically, this is achieved by adding temporal intervals  $T = 2\pi/\Delta\omega$ , with  $\Delta\omega$  being the angular frequency step. The analysis uses complex angular frequencies, where  $\omega_c = \omega + i\zeta$ , with  $\zeta = 0.7\Delta\omega$  to avoid the aliasing phenomena. In the time domain, this shift is later taken into account by applying an exponential window  $e^{\zeta t}$  to the response.

### 3 Case study

The methodology devised in this work is applied to a single edge notched beam of small size composed of normal concrete with maximum aggregate size of 8mm (see experimental details in [12]). The beam measures  $400 \times 100 \times 100 \text{ mm}^3$ , and has a  $5 \times 20 \times 100 \text{ mm}^3$  notch located at the top, as shown in Figure 5a. The material parameters are: Young's modulus  $E = 35000 \text{ N/mm}^2$ ; Poisson ratio  $\nu = 0.15$ ; tensile strength  $f_{t0} = 3.0 \text{ N/mm}^2$ ; and fracture energy  $G_F = 0.1 \text{ N/mm}$ . A constitutive law by [13] is adopted with normal stiffness  $k_n = 10^5 \text{ N/mm}^3$  and shear stiffness  $k_s = 4 \times 10^2 \text{ N/mm}^3$ .

A mesh composed of 474 bilinear elements is adopted (see Figure 5b). Loading is controlled using the arc-length method, in which the monotonic increase of the relative sliding displacement of the notch (Crack Mouth Slide Displacement - CMSD), is enforced. The discontinuity is constrained to propagate from the notch.

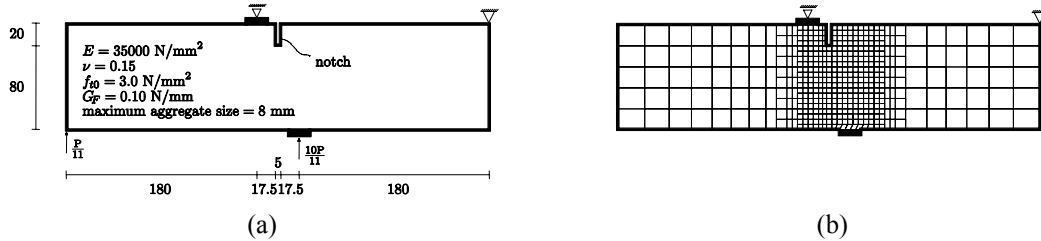


Figure 5: Single edge notched beam: (a) structural scheme (100 mm width, dimensions in mm); and (b) selected mesh.

The CMSD vs. load curve and obtained crack path are shown in Figure 6, from which it can be concluded that the numerical approach presents a good agreement with the experimental results. At the final stage of analysis the crack path shifts towards the inner support, detaching from the experimental results, due to an insufficient degree of discretisation at this area. However, for the stages selected for the propagation analysis of SH waves - see red dots in Figure 6a and deformed meshes represented in Figure 7 - this has no effect.

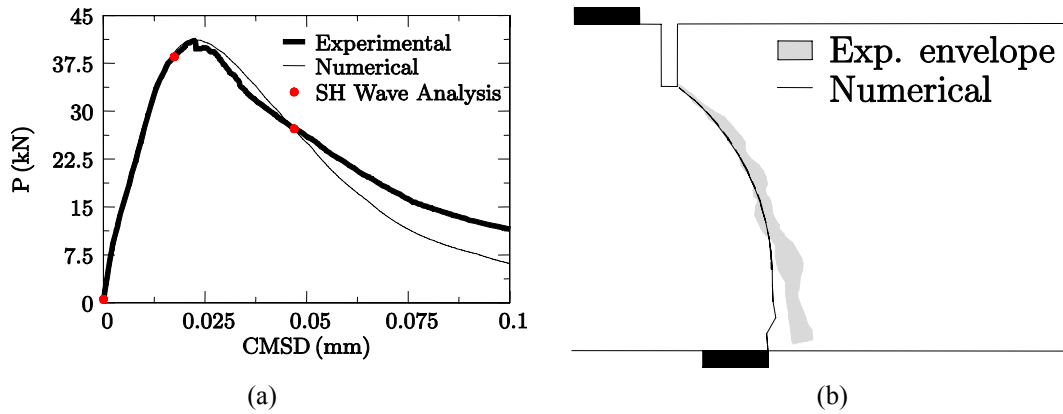


Figure 6: Single edge notched beam: (a) CMSD vs. load curves; and (b) crack path computed at CMSD = 0.1 mm.

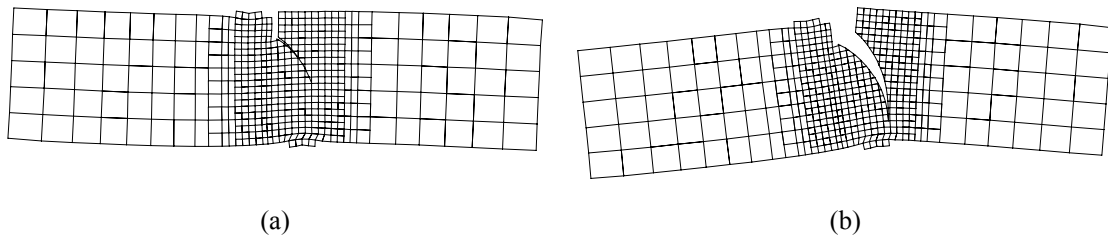


Figure 7: Single edge notched beam: deformed mesh (displacements amplified 250 times) for: (a) CMSD = 0.017 mm; and (b) CMSD = 0.047 mm.

After calculation of the crack propagation within the concrete beam, the crack path computed using the FEM model is used as the geometry input data for BEM. For the test case presented, three different stages are considered (see red dots in Figure 6a): the initial defect-free beam; the beam in cracked stage, with the crack tip 57 mm above the bottom (Figure 7a); and the cracked beam with the crack tip at 40 mm above the bottom of the beam (Figure 7b). Figures 8 to 10 illustrate the geometry of each model, together with the results calculated for a propagating Ricker pulse with a central frequency of 200 kHz, generated by a source positioned at (100 mm; 95 mm). For this calculation, 128 frequencies are used, ranging from 4000 Hz to 512000 Hz, with an interval of 4000 Hz. The wave propagation velocity considered for this case is of 2498.5 m/s, and the propagation medium was ascribed a density of 2500 kg/m<sup>3</sup>.

The time signals clearly reveal significant differences in the wave propagation pattern registered for the three cases. Particularly, the first wave arrival at the receivers reveals interesting features that can be used to infer the length of the crack. Indeed, this first arrival is generated by a diffraction effect at the crack tip (or at the bottom of the inset for the uncracked beam), and so it tends to occur at later times as longer cracks are considered (see schematic representation in Figure 11). This variation in the arrival times is mostly visible at receivers placed closer to the inset (left side of the plots). In addition, for longer cracks this diffraction effect originates a stronger deviation in the wave path, and thus a lower amount of energy reaches the

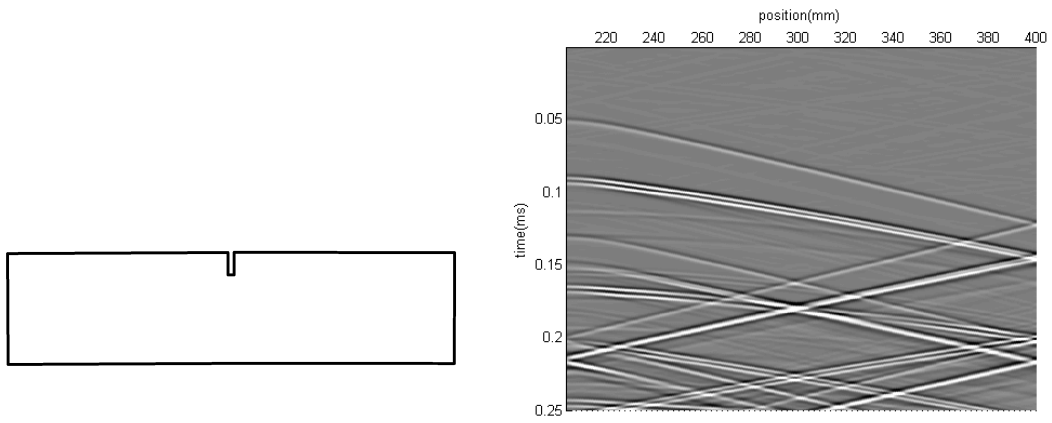


Figure 8: Results for propagating SH waves in an uncracked beam

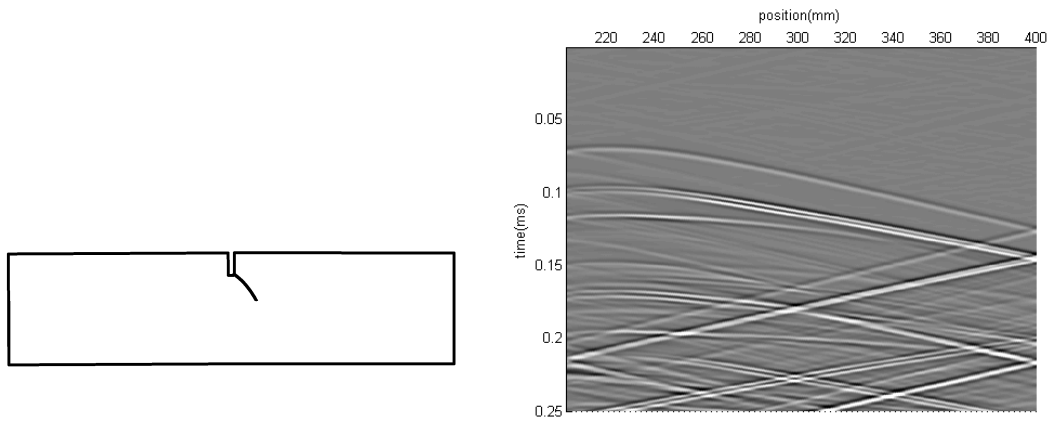


Figure 9: Results for propagating SH waves for the crack tip 57 mm above the bottom

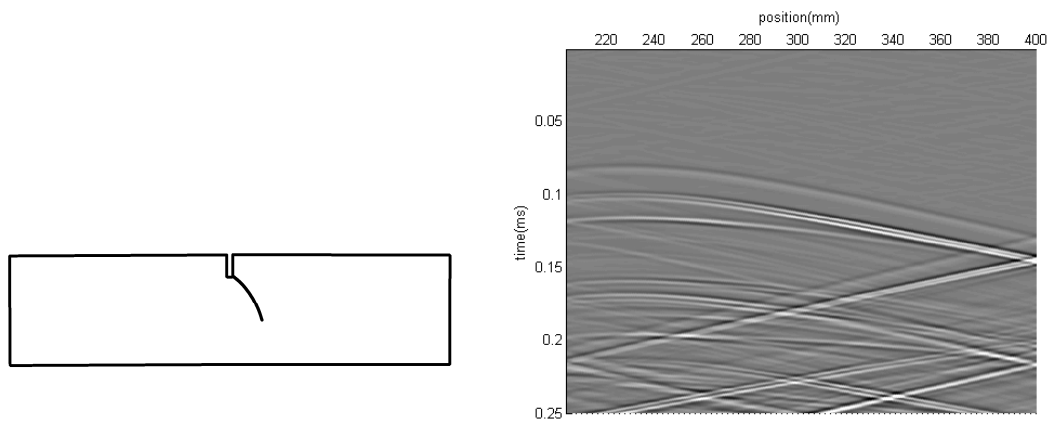


Figure 10: Results for propagating SH waves for the crack tip 40 mm above the bottom

receivers; this effect is also clearly visible in the plots. Interestingly, by analysing receivers placed further away from the inset, it also becomes clear that the second arrival suffers almost no changes for the three scenarios, arriving at the same time and with similar amplitude for the three cases. However, if the receivers placed closer to the inset are observed, a strong shadow effect originated by the presence of the crack can be identified.

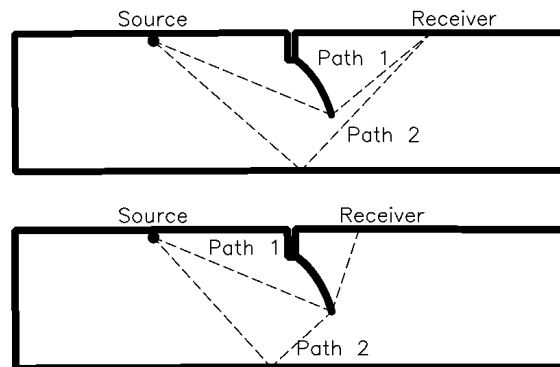


Figure 11: Illustrative sketch of the waves paths for the first two arrivals registered in the time signals.

## 4 Final remarks

The numerical approach devised by the authors followed a two-stage strategy: first, the process of crack propagation is analysed; and, then, the propagation of ultrasonic waves in the progressively damaged structure is addressed.

The tested case enabled the conclusion that the crack propagation model provided reliable results, accurately predicting the evolution of the crack within the structure. With respect to the crack identification by means of SH wave propagation patterns, the presented results allowed comparison of the effect of cracks with different lengths, helping in the identification of relevant differences in the time signals registered at receiver points located at the surface of the structure.

There are other relevant issues that have to be addressed, namely the influence of the presence of both aggregates and rebars.

## Acknowledgements

This research project has been funded by the Portuguese Science and Technology Foundation (FCT) with reference PTDC/ECM/098497/2008.

## References

- [1] M. Frizzarin, M. Feng, P. Franchetti, S. Soyos, C. Modena, “Damage detection based on damping analysis of ambient vibration data”, *Structural Control and Health Monitoring*, 17, 368-385, 2010.
- [2] D. Dias-da-Costa, J. Alfaiate, L.J. Sluys, E. Júlio, “An Embedded Discrete Strong Discontinuity Approach with Interelement Compatibility of the Enhanced Kinematical Field”, XI International Conference on Computational Plasticity Fundamentals and Applications, COMPLAS XI, Barcelona, Spain, 2011.
- [3] D. Dias-da-Costa, J. Alfaiate, L.J. Sluys, E. Júlio, “Towards a generalization of a discrete strong discontinuity approach”, *Computer Methods in Applied Mechanics and Engineering*, 198, 3670-3681, 2009.
- [4] D. Dias-da-Costa, J. Alfaiate, L.J. Sluys, E. Júlio, “A comparative study on the modelling of discontinuous fracture by means of enriched nodal and element techniques and interface elements”, *International Journal of Fracture*, 161, 97-119, 2010.
- [5] P. Santos, E. Júlio, J. Santos, “Towards the development of an in situ non-destructive method to control the quality of concrete-to-concrete interfaces”, *Engineering Structures*, 32, 207-217, 2010.
- [6] T. Michaels, J. Michaels, B. Mi, M. Ruzzene, “Damage detection in plate structures using sparse ultrasonic transducer arrays and acoustic wavefield imaging”, *Review of quantitative nondestructive evaluation*, Eds. D. Thompson, D. Chimenti, AIP, 24, 938-945, 2005.
- [7] T. Grahn, “Ultrasonic 2D SH crack detection in a layered anisotropic plate”, *Journal of Nondestructive Evaluation*, 20(1), 2001.
- [8] F. Cegla, “Ultrasonic Crack Monitoring Using SH Waves in extreme and inaccessible environments”, 17th World Conference on Nondestructive Testing, Shanghai, China, 2008.
- [9] A. Tadeu, P. Santos, E. Kausel, “Closed-form integration of singular terms for constant, linear and quadratic boundary elements - Part 1. SH wave propagation”, *Engineering Analysis with Boundary Elements*, 23(8), 671–681, 1999.
- [10] D. Soares Jr, L. Godinho, A. Pereira, C. Dors, “Frequency-domain analysis of acoustic wave propagation in heterogeneous media considering iterative coupling procedures between the Method of Fundamental Solutions and the Kansa’s Method”, *International Journal of Numerical Methods in Engineering*, 89(7), 914–938, 2012.
- [11] J. Alfaiate, G.N. Wells, L.J. Sluys, “On the use of embedded discontinuity elements with crack path continuity for mode-I and mixed-mode fracture”, *Engineering Fracture Mechanics*, 69(6), 661–686, 2002.
- [12] E. Schlangen, “Experimental and numerical analysis of fracture processes in concrete”, Ph.D. Thesis, Delft University of Technology, 1993.
- [13] G.N. Wells, L.J. Sluys, “Three-dimensional embedded discontinuity model for brittle fracture”, *International Journal of Solids and Structures*, 38(5), 897-913, 2001.